Supplementary information for

Consecutive intra-particle phase-transitions in the $LiFePO_4$ battery electrode material

Souzan Hammadi,[†] Nana Ofori-Opoku,[‡] Daniel Brandell,[†] and Peter Broqvist*,[†]

†*Department of Chemistry – Ångström Laboratory, Uppsala University, 75121 Uppsala, Sweden*

‡*Department of Materials Science and Engineering and Brockhouse Institute for Materials Research, McMaster University, Hamilton, L8S 1L4, Canada*

E-mail: peter.broqvist@kemi.uu.se

Contents

1 Model description

A phase-field model has been implemented that describes the phase evolution in the $LiFePO_4$ (LFP) battery electrode material. It is presented in our previous work in Ref.[1] and will be summarized herein. The model is based on the Cahn-Hilliard equation that describes the change in concentration driven by gradients of chemical potential.

$$\frac{\partial c}{\partial t} = \nabla \cdot [Mc(1-c)\nabla\mu] \,. \tag{1}$$

The mobility in turn depends on the Li diffusion coefficient, $M = DV_m/RT$, that is assumed to be isotropic. This coefficient corresponds to a 3 % antisite defect density which facilitates an isotropic Li diffusion pathway.[2,3] Note that a directional mobility description is possible and is explored in Section 8 of the Supplementary information.

The chemical potential is the variational derivative of a free energy functional $\mu = \partial F/\partial c$. The functional contains the following terms,

$$F = \int_V f_{chem} + f_{elast} + f_{grad} \; dV. \tag{2}$$

The first term (f_{chem}) describes the thermodynamic free energy, the second (f_{elast}) is the elastic energy contribution and the third (f_{grad}) describes the energy contribution of the interface.

Free energy description

The thermodynamic free energy is usually defined by the regular solution model,

$$f_{chem} = H^{excess} - TS^{ideal}_{conf} = \Omega/V_m c(1-c) + RT/V_m[c\,\ln c + (1-c)\ln(1-c)]. \tag{3}$$

Here, the entropic contribution S is assumed to be ideal and the non-ideality comes in

through the excess energy, i.e., the enthalpy. This enthalpic contribution is parameterized by Ω, which in theory, accounts for non-ideal interactions between species.

It is this contribution to the energy functional that is investigated in this work. The free energy descriptions of the LFP system available in the literature are presented in Figure 1.

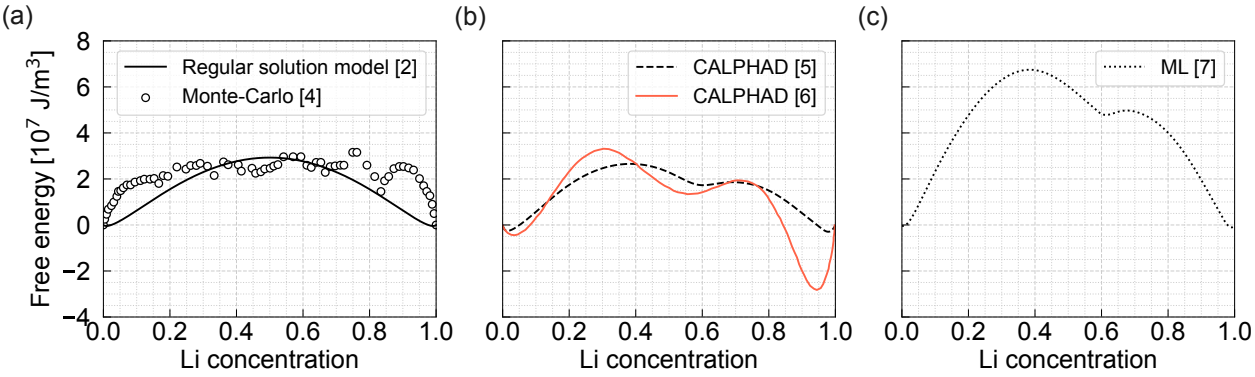

Figure 1: The free energy descriptions for the LFP system at room temperature from a) the regular solution model parameterized on Monte-Carlo data from Ref.,[2,4] b) two CALPHAD descriptions, one from the database by Phan et. al.[5] and one by van der Ven[6] and c) a fitting procedure aided by machine learning on experimental phase diagrams by Lund et al.[7]

This paper evaluates the phase evolution using three free energy descriptions: (i) the regular solution model, (ii) the free energy from the CALPHAD database by Phan et al.[5] and (iii) the optimized free energy using machine learning by Lund et al.[7]

Elastic contribution

The elastic contribution describes the coherency strain between the LFP and FP phase. Both these phases have orthorhombic symmetry (with space group Pnma), and so no major crystallographic rearrangement will occur during Li insertion and extraction. However, the Li will occupy octahedral sites in the FP lattice which causes volume expansion of the structure and thereby the development of coherency strain. This contribution is described by linear elasticity and is anisotropic due to the varying eigenstrains, ε.

$$f_{el} = \frac{1}{2} C_{ijkl}(\varepsilon_{ij} - \varepsilon^0_{ij} c)(\varepsilon_{kl} - \varepsilon^0_{kl} c) \tag{4}$$

In Eq. (5), C_{ijkl} is the stiffness matrix. In contrast, the elastic energy contribution has

the following form for an isotropic solid,[8]

$$f_{el}^{isotropic} = \frac{En^2}{1-\upsilon}(c-c_0)^2, \tag{5}$$

where E is Young's modulus and υ is Poisson's ratio. The parameter n defines the linear expansion per unit composition change and is calculated as $\frac{V_{LFP}-V_{FP}}{V_{LFP}}$, defined from the lattice constants of each crystal structure respectively.[9] This isotropic strain energy contribution is shown in Figure 1 of the paper to visualize the effect on the energy landscape.

The variable stress field (σ) can be solved assuming instantaneous mechanical equilibrium, i.e.,

$$\frac{\partial \sigma_{ij}}{\partial x_j} = \frac{\partial}{\partial x_j}[C_{ijkl}(\epsilon_{kl} - \epsilon_{kl}^0 c)] = 0. \tag{6}$$

A two dimensional system is established through a plane strain condition, assuming the eigenstrains $\varepsilon_{zz} = \varepsilon_{xz} = \varepsilon_{yz} = 0$.

Gradient energy

The gradient energy contribution is defined as,

$$f_{grad} = \frac{\kappa}{2}|\nabla c|^2, \tag{7}$$

where κ is the gradient energy coefficient defined as $\kappa = \sigma/L$. The parameter σ is the interfacial energy and L is the interface width.

Mobility description

Fundamentally, the relation between the diffusion coefficient and mobility comes from Fick's law that is defined as,

$$J = -D\frac{\partial c}{\partial y} \tag{8}$$

for a dilute solution and

$$J = -M\frac{\partial \mu}{\partial y} \tag{9}$$

for more concentrated solutions. However, $\delta\mu/\delta y = \delta\mu/\delta c\delta \cdot \delta c/\delta y$. And so the diffusion coefficient and mobility can be related as,[10]

$$D = M\frac{\partial \mu}{\partial c} \rightarrow M = \frac{D}{\partial \mu/\partial c} = \frac{D}{\partial^2 f/\partial c^2}. \tag{10}$$

2 Boundary conditions and electrochemical metrics

The simulated single-particle system is illustrated in Figure 2 below.

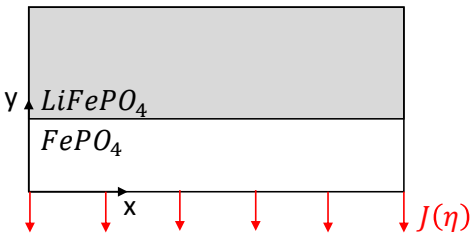

Figure 2: Schematic illustration of the simulated system showing the (0 1 0) and (1 0 0) surfaces as well as the charge transfer flux condition marked in red. x and y stand for the [1 0 0] and [0 1 0] direction respectively.

Traction-free boundary conditions are applied on the (0 1 0) surfaces and zero-displacement conditions on the (1 0 0) surfaces. Furthermore, periodic boundary conditions are applied in the [1 0 0] direction.

The Cahn-Hilliard equation that determines the change in concentration over time, presented in equation 1, contains second- and fourth-order spatial derivatives which requires higher order shape functions in FEM. In order to avoid that, the expression is split into two coupled equations to be solved separately. These two coupled equations correspond to the following,

$$\frac{\delta c}{\delta t} = \nabla \cdot (M\nabla\mu) \ \texttt{and} \ \mu = \frac{\delta f}{\delta c} - \kappa\Delta c \tag{11}$$

The weak form of the first part of equation (11) contains integral terms, where the last one concerns the surface S while the other represents the bulk.

$$\int_V w \cdot M\nabla \cdot \nabla\mu dV = -\int_V M\nabla w \cdot \nabla\mu dV + \int_{\delta V} M\nabla\mu \cdot w\hat{n} \cdot dS \tag{12}$$

Here, w is the test function used in the finite element solution. As such, to naturally induce a flux in a consistent manner, the rate of Li removal is connected to the chemical potential of the system which is conventionally done using the Butler-Volmer equation. In this work, the Marcus-Hush-Chidsey (MHC) model for electron transfer is used instead, as it has been shown that the LFP system is dominantly governed by electron transfer rather than iconic transfer.[11] Inducing charge transfer at the bottom boundary of the simulation box is done by introducing a flux in concentration with a Neumann boundary condition. The MHC equation by Zeng et al. is used,[12] where the rate is defined as $J(\eta) = j_0(k_{ox}(-\eta) - k_{red}(\eta))$ leading to,

$$J(\eta) \approx \tau \cdot j_0\sqrt{\pi\lambda}\left(\frac{e^{\eta} - e^{-\eta}}{e^{\eta} + e^{-\eta} + 2}\right)\mathrm{erfc}\left(\frac{\lambda - \sqrt{1 + \sqrt{\lambda} + \eta^2}}{2\sqrt{\lambda}}\right), \tag{13}$$

where j_0 is the exchange current density, λ is the reorganizational energy and η is the overpotential. The parameter τ is used to adjust the equation to the Tafel limit at low overpotentials. Note that, the previously used form $\tanh(\eta/2)$ was a typographical error and does not correspond to the correct expression $\left(\frac{e^{\eta}-e^{-\eta}}{e^{\eta}+e^{-\eta}+2}\right)$; the results remain unaffected.[1,12]

The exchange current density j_0, is related to the rate constant k according to,

$$j_0 = \frac{nF}{N_A L^2}k, \tag{14}$$

where n is the number of transferred electrons for each Li ion, F is Faraday's constant and N_A is Avogadro's number and L is the interface width. The overpotential in turn is the difference between the electrode potential at equilibrium ($E_{eq} = \mu_{eq}$) and during operation ($E = \mu - F\Delta\Phi$) with an applied potential $\Delta\Phi = 100\ mV$.

$$\eta = E_{eq} - E = \mu_{eq} - \mu - F\Delta\phi \tag{15}$$

The applied potential brings the system out of equilibrium, resulting in a changing current with the delithiation process. The cell potential is the difference between the electrode potential and a reference, in this case Li ($E_{Li} = -3.04$ V).

$$E_{cell} = E^{Li}_{LFP} - E^{Li}_{Li} = \left(\frac{\mu}{F} + \Delta\Phi\right) - E^{Li}_{Li} \tag{16}$$

Note that the cell in this case is the simulated single-particle domain represented by Figure 2. The current of this set-up is then defined as the integral over the concentration change at the boundary, S, where charge transfer is occurring,

$$I = \frac{F}{N_A L_S} \int_S \frac{\partial c}{\partial t} dS, \tag{17}$$

where L_S is the length of the surface. The varying chemical potential in the system (μ) induces a changing overpotential (η) resulting in a varying current during Li extraction. Although the external potential ($\Delta\Phi$) is constant, the intrinsic particle potential (μ) evolves as Li is removed. Consequently, the system does not remain globally at a constant voltage which is commonly referred to as a potentiostatic condition, since only the applied potential is fixed.

The mechanism for Li extraction in this model is different from typical battery operation conditions where battery cells are typically driven under galvanostatic conditions (constant current), resulting in an overall uniform Li flux over the entire electrode. In such a scenario, Li extraction occurs dynamically across hundreds of active particles, either simultaneously or sequentially, to collectively sustain the imposed current. These heterogeneously distributed processes pose significant challenges for modeling single-particle systems under mass transport limitations. A constant current condition, while useful and interesting, would require additional assumptions on the model and/or additional complexity in the solution, like ad-

justing the applied potential at each iteration.[13] In the study by Bai et al.,[13] it is assumed that the Li enters the system through a surface insertion mechanism thereby allowing the concentration at the interfaces within the bulk to reach that of the surface of the particle. This allows Li to be inserted or extracted at a constant rate. This assumption holds well for nano-scale particles, where the surface-to-volume ratio is high, but becomes less valid for larger particles.

In larger particles, mass transport limitations play a greater role. As the FP phase develops from the electrode/electrolyte interface and progresses into the bulk, fewer Li ions can reach the interface for charge transfer. This results in a varying current rather than a constant one.

3 Parameters and simulation conditions

Table 1: Parameters utilized in modeling Li deintercalation in $LiFePO_4$.

Parameter	Description	Value	Source
V_m	Molar volume	4.38×10^{-5} m^3/mol	[2]
Ω	Regular solution coefficient	12×10^3 J/mol	[2]
T	Temperature	298 K	-
R	Gas constant	8.3145 J/mol·K	-
D	Diffusion coefficient	1×10^{-15} m^2/s	[2]
σ	Interfacial energy	0.072 J/m^2	[2,14]
μ_{eq}	Equilibrium chemical potential	-2.11×10^{-5} J/m^3	-
$\Delta\phi$	Applied potential	100 mV	-
L	Interface width/length unit	1 nm	-
$\epsilon^0_{11}, \epsilon^0_{22}, \epsilon^0_{33}$	Eigenstrains (LFP as reference)	5.0 %, 3.6 %, -1.9 %	[2,15]
E	Young's modulus	125.7×10^9 Pa	[2]
ν	Poisson's ratio	0.252	[2,16]
n	linear expansion parameter	0.04	[1,9]
k_0	Rate constant	2.062×10^{-4} s^{-1}	[11]
λ	Reorganizational energy	8.3RT J/mol	[11]
τ	Correction parameter	3.358	[1]

The elements in the stiffness matrix are,

$$C_{11} = \lambda\frac{1-\nu}{\nu}, \quad C_{12} = \lambda \quad \text{and} \quad C_{44} = \lambda\frac{1-2\nu}{2\nu}. \tag{18}$$

The Lamé constant, λ, is defined using Poisson's ratio, ν, and Young's modulus, E,

$$\lambda = \frac{E\nu}{((1+\nu)(1-2\nu))}. \tag{19}$$

The stiffness matrix is thus defined as,

$$C_{2D} = \begin{bmatrix} C_{11} & C_{12} & 0 \\ C_{12} & C_{11} & 0 \\ 0 & 0 & C_{44} \end{bmatrix} \tag{20}$$

Note that it is possible to define the stiffness matrix completely from first principle calculations, however this results in only minor differences in the resulting microstructure. [2]

To induce higher charge transfer rates, the magnitude of the rate constant is varied in our simulation study, up to $k = 2.062 \times 10^5$ s^{-1}, giving $k/k_0 = 10^5$. The experimental rate constant from Ref. [11] is not entirely transferable to our simulation, where in reality the LFP electrode consists of a complex porous multi-particle architecture and the other is a single particle simulation thus motivating the use of charge transfer rates at different order of magnitude.

All the equations are non-dimensionalized and scaled using an energy barrier defined as $H = \sigma/L$, the length scale L = 1 nm and time-scale $t = L^2/D$.

4 Spline interpolations and validation

The python package for symbolic computing, Sympy, is used to generate the spline functions. [17] In the case of the CALPHAD and ML models, data have been extracted from Figure 3 in Ref. [7] Due to the lack of finely spaced datapoints, a smoothing procedure is first employed using the python package Scipy.

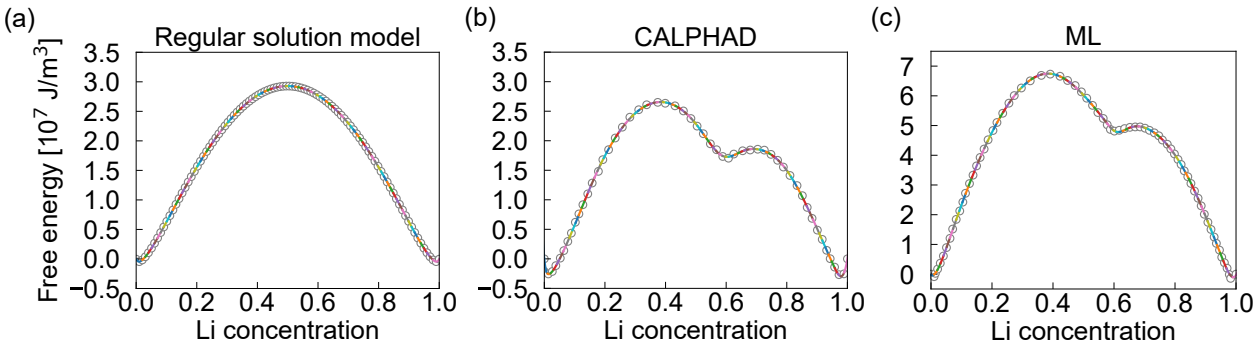

Figure 3: Datapoints and spline interpolations of a) the regular solution model, b) CALPHAD free energy by Phan et al.[5] and c) ML generated free energy by Lund et al.[7] Note the different scaling on the y-axis.

As a proof of concept, we implement and test the spline function for the regular solution model. The phase-field simulations are shown in Figure 4. The exact same results are obtained using the spline as for the functional form. This validates the chosen approach.

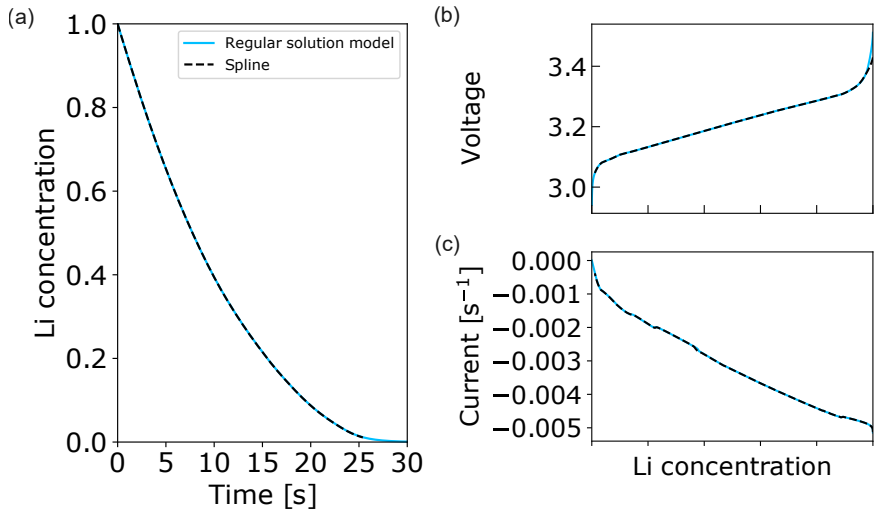

Figure 4: Reproducing results using the regular solution model, by spline or functional form as a proof of concept. a) The change in Li concentration over time, b) the voltage and c) the current I/FN_A.

5 Phase-field simulations without coherency strain

Phase-field simulations conducted without coherency strain and presented in Figure 5 showing the decrease in average Li concentration over time, voltage, current and snapshots of the

simulated microstructure. The simulation using the ML description stalled at 97% Li, likely due to the high energy barrier.

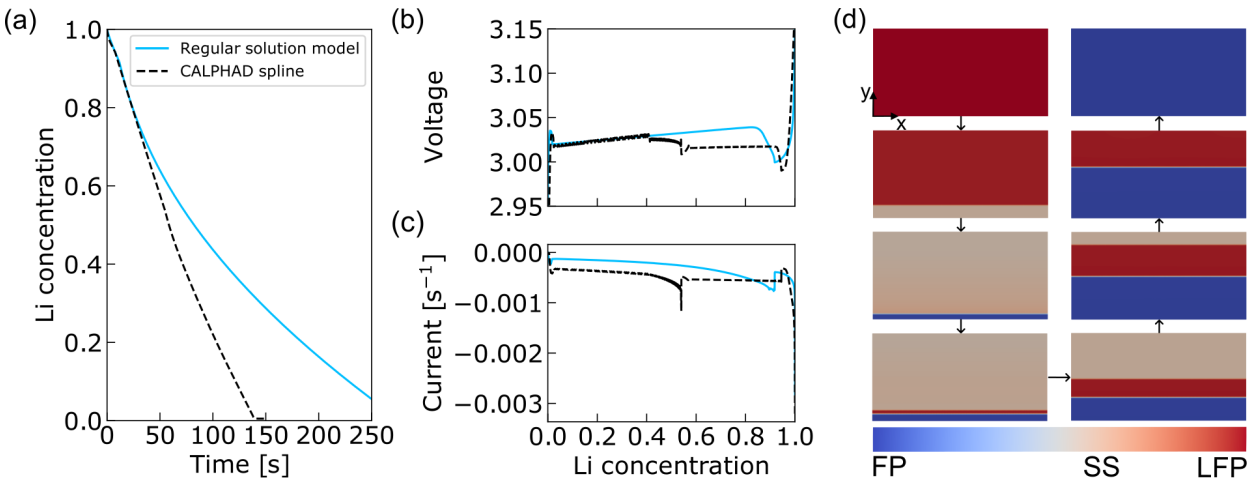

Figure 5: Phase-Field simulations of a delithiation process in an LFP system without coherency strain at charge transfer rate $k/k_0 = 10^4$ showing a) the change in average Li concentration over time, b) the voltage profile, c) the current I/FN_A and d) snapshots from the phase-field model (128x64 nm) taken at different times using the CALPHAD free energy description. The snapshots show the start (fully LFP = red) and end (fully FP = blue) of the delithiation process. SS stands for solid solution.

In the simulation using the CALPHAD free energy, the Li concentration decreases more rapidly than in the regular solution model, as shown in Figure 5a, despite all other parameters remaining constant. The discontinuity in the voltage profile is attributed to a first-order phase transition that is characterized by nucleation and subsequent growth.[1] Notably, both the voltage and current exhibit three discontinuities, one around 95 %, one at roughly 50-60% Li content and the other at 40%, suggesting that three phase transitions take place during the delithiation process.

Snapshots from the simulations presented in Figure 5d using the CALPHAD energy input illustrate that the system starts with 100 % Li with LFP. The delithiation then proceeds with the initiation of a phase containing approximately 60% Li, the first phase transition. This phase corresponds to the metastable solid solution phase in the energy landscape shown in Figure3b, which is denoted SS. Once this phase has completely filled the simulation box, the FP phase is initiated at the second phase transition. The initiation of the FP phase

corresponds to the second discontinuity observed in the voltage profile, at roughly 50-60% Li concentration in Figure 5b, with delithitation progressing through the motion of the SS/FP interface. Subsequently, the concentration of Li at the SS/FP interface increases, allowing the LFP phase to reemerge which results in the third discontinuity in the voltage profile, at around 40 % Li (see Figure 5b). When the mobility of the SS/FP front is limited, the formation of a sharper LFP/FP interface becomes energetically favorable due to the steeper concentration gradient. Ultimately, the delithiation proceeds though the coordinated movement of all three phases.

6 Phase-field simulations at low charge transfer rates

To evaluate the effect of the charge transfer rate on the presence and evolution of the solid solution phase, simulations are also conducted at lower rate constants and presented in Figure 6.

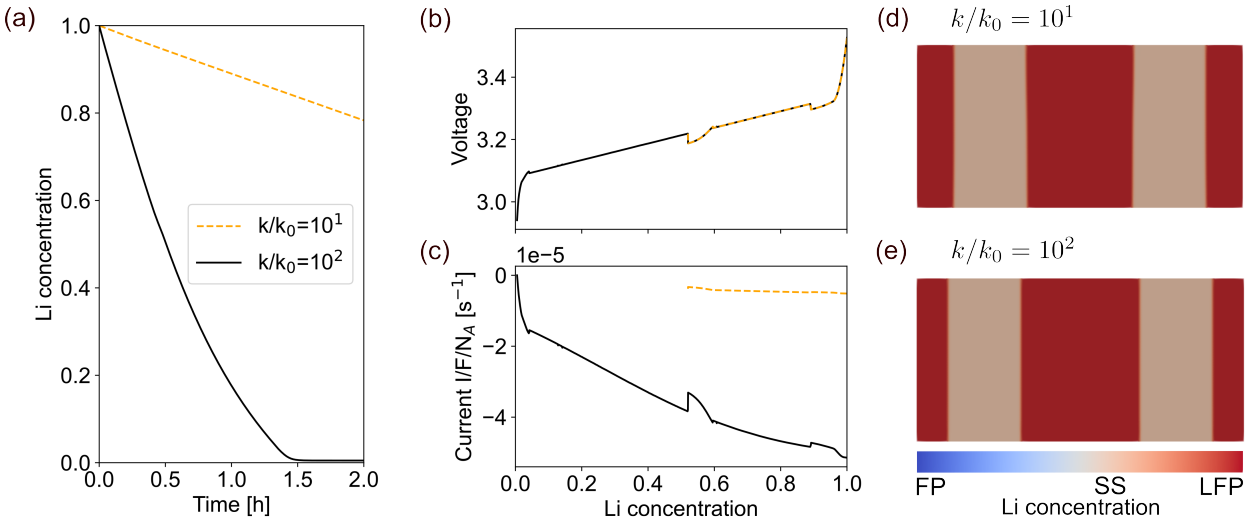

Figure 6: Phase-field simulations at charge transfer rate $k/k_0 = 10^2, 10^1$ using the CALPHAD free energy description showing a) change in Li concentration with time, b) change in voltage and c) change in current as well as snapshots at 80 % average Li concentration from the simulation at d) $k/k_0 = 10^1$ and e) $k/k_0 = 10^2$.

These results show the presence of the solid solution phase even at lower fluxes where the delithiation of a single-particle system of size 128x64 nm now takes hours instead of seconds

to complete. Thereby strengthening our conclusion that this phase is thermodynamically stabilized, whilst kinetics does induce variation in phase coexistence and morphology.

7 Comparison between 2D and 3D simulations

2D simulations simplify computations by employing a plane strain assumption, i.e. $\varepsilon_{zz} = \varepsilon_{xz} = \varepsilon_{yz} = 0$, thereby enabling quicker calculation times. However, variations in the strain along the third dimension might influence stress distribution and, consequently, the energy landscape. To confirm that the observed three phase evolution is not an artifact of the 2D model setup, we conduct simulations considering also strain in the z-direction. This renders the following stiffness matrix.

$$C_{3D} = \begin{bmatrix} C_{11} & C_{12} & C_{12} & 0 & 0 & 0 \\ C_{12} & C_{11} & C_{12} & 0 & 0 & 0 \\ C_{12} & C_{12} & C_{11} & 0 & 0 & 0 \\ 0 & 0 & 0 & C_{44} & 0 & 0 \\ 0 & 0 & 0 & 0 & C_{44} & 0 \\ 0 & 0 & 0 & 0 & 0 & C_{44} \end{bmatrix} \tag{21}$$

To limit the computational demand that arises from conducting 3D simulations, the size of the system is reduced to 64x32x32 nm in 3D and 64x32 nm in 2D. Snapshots of these simulations at varying rate constants are shown in Figure 7.

The size effect is prominent when comparing these 2D simulations to those presented in the paper. The phase evolution is similar in 2D as well as 3D and both simulations show the initiation and evolution of a solid solution phase. This confirms the presence of the solid solution phase as not an artifact from the plane strain assumption.

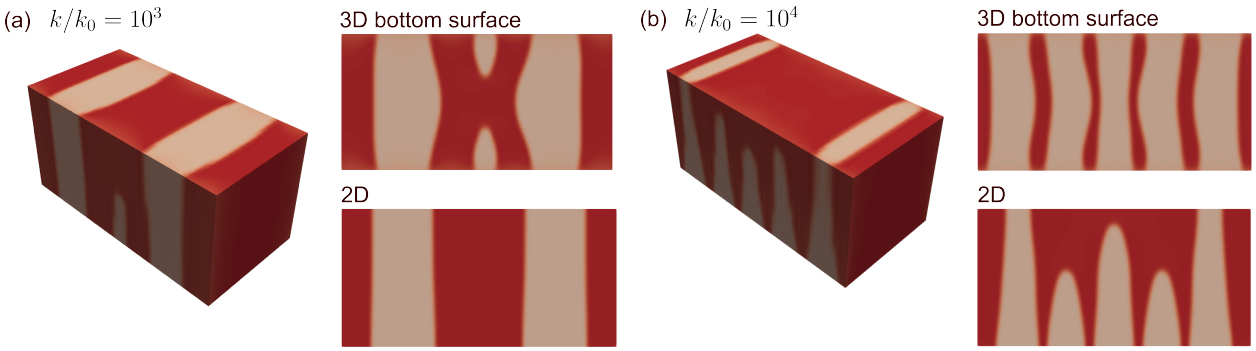

Figure 7: Phase-field simulations in 3D (64x32x32 nm) and 2D (64x32 nm) at charge transfer rate a) $k/k_0 = 10^3$ and b) $k/k_0 = 10^4$ showing snapshots at 80 % average Li concentration from the 3D simulation, the bottom surface of the 3D simulation and the 2D simulation.

8 The case of anisotropic mobility

A defect-free LFP crystal showcases highly anisotropic diffusion in the y-direction.[18] This section explores wether the solid solution phase evolves even under highly anisotropic diffusion. To test the effect of such anisotropy on the evolution of the solid solution phase, we conduct 2D simulations assuming negligible diffusion in the x-direction. This gives the mobility tensor,

$$\mathbf{M}(c) = c(1-c)\frac{V_m}{RT}\begin{bmatrix} 0 & 0 \\ 0 & D \end{bmatrix}. \tag{22}$$

Note that the value for the diffusion constant D that is used in the phase-field simulations represents a system at 3% antisite defect density,[2,3] wether a complete defect free system would have a different diffusion constant. Once again, to limit the computational demand, simulations with smaller domain size (64x32 nm) are conducted. Phase-field simulations for the case of isotropic mobility M_{xy} and anisotropic mobility M_y are presented in Figure 8.

While the time evolution in the system is the same, the phase boundary morphology differs depending on the assumption on the Li mobility. The more planar interface implies the kinetics overcoming the anisotropic coherency strain and resemble more closely the planar interface presented by in-situ TEM studies.[19]

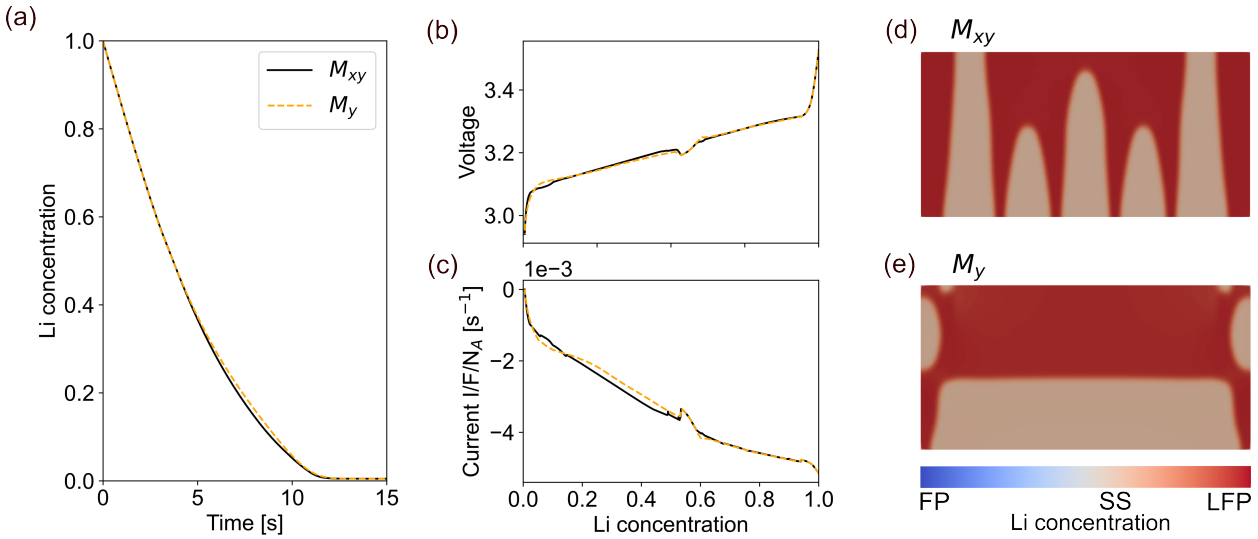

Figure 8: Phase-field simulations for charge transfer rate $k/k_0 = 10^4$ and size 64x32 nm using the CALPHAD free energy description showing a) change in Li concentration with time, b) change in voltage and c) change in current as well as snapshots at 80 % average Li concentration from the simulation at d) isotropic mobility M_{xy} and e) Li mobility only in the y direction M_y.

Both simulations showcase the presence of the solid solution phase. Including such anisotropic material properties, not only for mobility but also gradient energies, might be necessary to obtain qualitative data on phase evolution in the LFP material. For the mobility description, this will require diffusion data and/or knowledge about the defect density. Additionally including anisotropic gradient energies would require the inclusion of an order parameter to explicitly model all three phases separately, and could be done by coupling the system with an Allen-Cahn equation.

References

(1) Hammadi, S.; Broqvist, P.; Brandell, D.; Ofori-Opoku, N. Investigation of charge transfer models on the evolution of phases in lithium iron phosphate batteries using phase-field simulations. *Journal of Materials Chemistry A* **2025**,

(2) Yang, K.; Tang, M. Three-dimensional phase evolution and stress-induced non-uniform

Li intercalation behavior in lithium iron phosphate. *Journal of Materials Chemistry A* **2020**, *8*, 3060–3070.

(3) Hong, L.; Li, L.; Chen-Wiegart, Y.-K.; Wang, J.; Xiang, K.; Gan, L.; Li, W.; Meng, F.; Wang, F.; Wang, J.; Chiang, Y.-M.; Jin, S.; Tang, M. Two-dimensional lithium diffusion behavior and probable hybrid phase transformation kinetics in olivine lithium iron phosphate. *Nature Communications* **2017**, *8*.

(4) Malik, R.; Zhou, F.; Ceder, G. Kinetics of non-equilibrium lithium incorporation in $LiFePO_4$. *Nature Materials* **2011**, *10*, 587–590.

(5) Phan, A. T.; Gheribi, A. E.; Chartrand, P. Modelling of phase equilibria of $LiFePO_4$-$FePO_4$ olivine join for cathode material. *The Canadian Journal of Chemical Engineering* **2019**, *97*, 2224–2233.

(6) Van der Ven, A.; Garikipati, K.; Kim, S.; Wagemaker, M. The Role of Coherency Strains on Phase Stability in Li_xFePO_4: Needle Crystallites Minimize Coherency Strain and Overpotential. *Journal of The Electrochemical Society* **2009**, *156*, A949.

(7) Lund, J.; Wang, H.; Braatz, R. D.; García, R. E. Machine learning of phase diagrams. *Materials Advances* **2022**, *3*, 8485–8497.

(8) Cahn, J. W. On spinodal decomposition. *Acta Metallurgica* **1961**, *9*, 795–801.

(9) Hammadi, S.; Kullgren, J.; Wolf, M. J.; Brandell, D.; Broqvist, P. Impact of temperature on short-range charge ordering in $LiFePO_4/FePO_4$. *Physical Review B* **2024**, *109*, 144103.

(10) Moelans, N.; Blanpain, B.; Wollants, P. An introduction to phase-field modeling of microstructure evolution. *Calphad: Computer Coupling of Phase Diagrams and Thermochemistry* **2008**, *32*, 268–294.

(11) Bai, P.; Bazant, M. Z. Charge transfer kinetics at the solid–solid interface in porous electrodes. *Nature Communications 2014 5:1* **2014**, *5*, 1–7.

(12) Zeng, Y.; Smith, R. B.; Bai, P.; Bazant, M. Z. Simple formula for Marcus–Hush–Chidsey kinetics. *Journal of Electroanalytical Chemistry* **2014**, *735*, 77–83.

(13) Bai, P.; Cogswell, D. A.; Bazant, M. Z. Suppression of Phase Separation in $LiFePO_4$ Nanoparticles During Battery Discharge. *Nano Letters* **2011**, *11*, 4890–4896.

(14) Abdellahi, A.; Akyildiz, O.; Malik, R.; Thornton, K.; Ceder, G. Particle-size and morphology dependence of the preferred interface orientation in LiFePO 4 nano-particles. *Journal of Materials Chemistry A* **2014**, *2*, 15437–15447.

(15) Meethong, N.; Huang, H. Y. S.; Speakman, S. A.; Carter, W. C.; Chiang, Y. M. Strain Accommodation during Phase Transformations in Olivine-Based Cathodes as a Materials Selection Criterion for High-Power Rechargeable Batteries. *Advanced Functional Materials* **2007**, *17*, 1115–1123.

(16) Hill, R. The Elastic Behaviour of a Crystalline Aggregate. *Proceedings of the Physical Society. Section A* **1952**, *65*, 349.

(17) Meurer, A.; Smith, C. P.; Paprocki, M.; Čertík, O.; Kirpichev, S. B.; Rocklin, M.; Kumar, A.; Ivanov, S.; Moore, J. K.; Singh, S.; others SymPy: symbolic computing in Python. *PeerJ Computer Science* **2017**, *3*, e103.

(18) Islam, M. S.; Driscoll, D. J.; Fisher, C. A. J.; Slater, P. R. Atomic-Scale Investigation of Defects, Dopants, and Lithium Transport in the LiFePO4 Olivine-Type Battery Material. *Chemistry of Materials* **2005**, *17*, 5085–5092.

(19) Niu, J.; Kushima, A.; Qian, X.; Qi, L.; Xiang, K.; Chiang, Y.-M.; Li, J. In Situ Observation of Random Solid Solution Zone in $LiFePO_4$ Electrode. *Nano Letters* **2014**, *14*, 4005–4010.